CHAPTER-6

Effects of MnO_2 Crystal Phases in MnO_2/CeO_2 Catalyst for NO Reduction by NH_3-SCR

Abstract

The MnO_x-based catalysts showed excellent catalytic activity at low temperatures for the NH_3-SCR reaction due to their high concentration of labile oxygen sites, essential for completing the reduction cycle required for catalysts. Among the different species of MnO_x, MnO_2 has shown a significant effect on the SCR reaction due to the high oxidation capacity of Mn^{4+} at low temperatures. It has been observed that the phase structure of MnO_2 can also largely influence the NH_3-SCR performance. As MnO_2 exists in different phases, including α-, β-, δ- and γ, in which MnO_6 octahedral units are linked in either a tubular or layered structure. Furthermore, the catalytic activity of MnO_x supported on various transition metal oxides (TiO_2, ZrO_2, CeO_2, Al_2O_3) has shown high performance for low-temperature SCR catalysts. [1-2]

In the previous chapter, we synthesized the MnO_2, Mn_2O_3, and MnO oxides, which were impregnated on CeO_2-NR support and used for NO removal using the NH_3-SCR. Among all the catalysts, MnO_2-CeO_2-NR gave the best performance. In this chapter, we have synthesized different crystal structures of MnO_2 and impregnated on the CeO_2-NR using the wet-impregnation method. Further, these catalysts were characterized through BET, XRD, XPS, SEM-EDX, TEM and Raman spectroscopy. Finally, the activity of these catalysts was analyzed for the NO reduction.

6.1. Experimental

6.1.1. Materials and methods

All the reagents and gases used in the study were purchased commercially and were used without further purification. The chemicals used were cerium (III) nitrate hexahydrate ($Ce(NO_3)_3.6H_2O$, 99 % purity, SRL Pvt. Ltd), sodium hydroxide (NaOH, 98 % purity, biochemika), ethanol (99% purity, SD fine-chemical limited), potassium permanganate ($KMnO_4$, 99% purity, Sigma Aldrich), manganese sulfate monohydrate ($MnSO_4.H_2O$, 99% purity, Sigma Aldrich), and ammonium persulfate ($(NH_4)_2S_2O_8$, 97% purity, Sigma Aldrich).

6.1.2. Support preparation

The CeO_2-Nanorod was synthesized using the hydrothermal method. For this, $Ce(NO_3)_36H_2O$ (2.17 gm) in 20 ml of deionized water and NaOH (15.4 gm) in 55 ml of deionized water were dissolved separately and later mixed to form a homogeneous solution. This homogenous solution was then transferred into a stainless-steel autoclave lined with Teflon and kept in the oven at 100°C for 5 h for the hydrothermal process. The obtained precipitate found was then washed several times with deionized water and ethanol to remove any potential ionic contaminants. The washed precipitate was then filtered using vacuum filtration, and dried in oven at 80°C for 12h. The dried sample was further calcined at 500°C for 5h. The obtained sample was denoted as CeO_2-NR in the manuscript.

6.1.3. Catalysts preparation

All the phases of MnO_2 were synthesized by the hydrothermal method. The α-MnO_2 phase was synthesized by mixing 1.2 gm of $KMnO_4$ in 60 ml of deionized water with 0.5 gm of $MnSO_4.H_2O$ for 30 minutes at ambient temperature under magnetic stirring until the homogenous solution is formed. Afterward, homogeneous solutions were put into a 100 ml Teflon-lined stainless-steel autoclave, sealed, and kept at 140°C for 12 h. The obtained

precipitate was later washed several times with deionized water and ethanol to remove any undesirable ions. The washed precipitate was then filtered using vacuum filtration, and dried in oven at 105°C for 12h. The β-MnO_2 phase was synthesized by taking 0.5 gm of $KMnO_4$ and 2.5 gm of $MnSO_4.H_2O$, while for the δ-MnO_2 phase, 2.8 gm of $KMnO_4$ and 0.5 gm of $MnSO_4.H_2O$ were taken and the other conditions were same as the α- MnO_2. The γ-MnO_2 phase was synthesized by mixing 3.7 gm of $(NH_4)_2S_2O_8$ with 2.7 gm of $MnSO_4$ for 30 minutes for a homogeneous mixture and transferred it into an autoclave at 90°C for 24 h. All the phases of MnO_2 were further calcined for 2 h at 300 °C. [3]

The wet-impregnation was used to load the different phases of MnO_2 on CeO_2-NR support. Active metals (5wt.%, 8wt.%, wt.11 %, wt.14 %, and wt.17 %) and CeO_2-NR support (1 gm) were mixed in deionized water and stirred until homogenous. The obtained solution was put in an oven for drying at 105°C for 12 h, followed by calcination at 350 °C for 4 h. The obtained catalysts were denoted as α-MnO_2/CeO_2-NR, β-MnO_2/CeO_2-NR γ-MnO_2/CeO_2-NR, and δ-MnO_2/CeO_2-NR.

6.2. Results and discussion

6.2.1. Brunauer–Emmett–Teller (BET)

The BET surface areas, pore volumes, and pore diameters of support and catalysts are summarized in **Table 6.1**. All the adsorption-desorption isotherms exhibited in all the synthesized samples are similar, as shown in **Fig. 6.1**, and they are categorized by the IUPAC as type IV isotherms, which are commonly observed in mesoporous materials. [4,5] The CeO_2-NR has 22.75 m^2-gm^{-1}, 0.11 cm^3-gm^{-1}, and 12.23 nm surface area, pore volume, and pore diameter respectively. The BET surface area, pore volume, and pore diameter of catalysts have all been reduced after the impregnation of different phases of MnO_2. The α-MnO_2/CeO_2-NR had the highest surface area of 21.22 m^2-gm^{-1}, while the β-MnO_2/CeO_2-NR had the lowest

surface area of 16.17 m^2-gm^{-1}. The order of decreasing surface area of the catalysts is α-MnO_2/CeO_2-NR < δ-MnO_2/CeO_2-NR < γ-MnO_2/CeO_2-NR < β-MnO_2/CeO_2-NR. The highest surface area is most probably due to the well dispersion of active metals on the supports, while the low surface may be due to the support's pore volume being blocked when impregnated the active metals. [6,7]

Table 6.1. BET data, average crystal size, and average particle size of the support and Catalysts

Sample	Surface area (m^2-gm^{-1})	Pore volume (cm^3-gm^{-1})	Pore diameter (nm)
CeO_2-NR	22.75	0.11	12.23
α-MnO_2/CeO_2-NR	21.22	0.08	9.32
β-MnO_2/CeO_2-NR	16.17	0.07	6.36
γ-MnO_2/CeO_2-NR	18.30	0.03	6.54
δ-MnO_2/CeO_2-NR	19.98	0.05	7.60

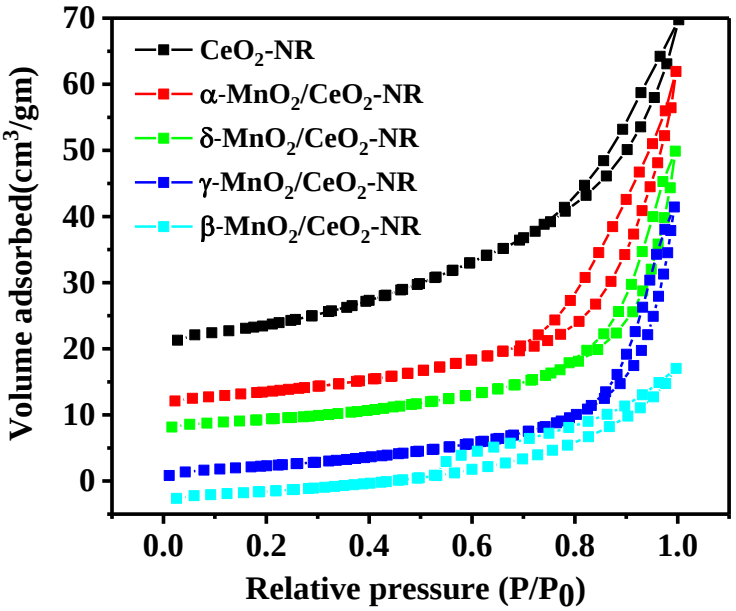

Fig.6.1. N_2 adsorption and desorption of ceria support and catalysts

6.2.2. X-Ray Diffraction *(*XRD)

The XRD characterization was performed to determine the phases of the ceria supports, active metals, and catalysts, as shown in **Fig.6.2.** All four samples of the MnO_2 phase displayed XRD patterns that can be accurately indexed shown in **Fig.6.2(a)**. The reflection peaks of α-MnO_2 (JCPDS 98-008-1700, tetragonal, a=b=9.8150, c=2.8470) were observed at 2θ values of 12.58°, 18°, 28.74°, 37.563°, 41.01°, 41.91°, 41.91°, 47.2°, 49.79°, 56.06°, 60.11°, 65.293°, 69.54°, and 72.76° corresponded to (111), (200), (310), (201), (301), (411), (600), (521), (002), and (541) planes respectively; for β-MnO_2 (JCPDS 98-000-5732, tetragonal, a=b=3.3980, c= 2.8730) peaks were noted at 2θ values of 28.69°, 37.37°, 41.01°, 42.78°, 46.18°, 56.66°, 59.35°, 64.918°, 67.22°, and 72.28° corresponded to (110), (101), (200), (111), (210), (211), (220), (002), (310), and (301) planes respectively; for γ-MnO_2 (JCPDS 98-003-5156, tetragonal, a=b=4.4040, c= 2.8770) peaks were observed at 2θ values of 26.32°, 37.07°, 42.59°, 56.41°, and 65.62° corresponded to (120), (131), (300), (160), and (003) planes respectively and for δ-MnO_2 (JCPDS 80-1098, monoclinic phase, a = 5.149 Å, b = 2.843 Å, and c = 7.176 Å) peaks were noted at 2θ values of 12.37°, 24.87°, 36.80°, and 65.5° corresponded to (001), (002), (200), and (020) planes respectively. The high intensities of α-MnO_2 and β-MnO_2 and their narrow peak widths suggested a crystallinity-rich composition. However, compared to α-MnO_2 and β-MnO_2, the diffraction peaks of γ- MnO_2 and δ-MnO_2 exhibit lower intensities and larger widths.

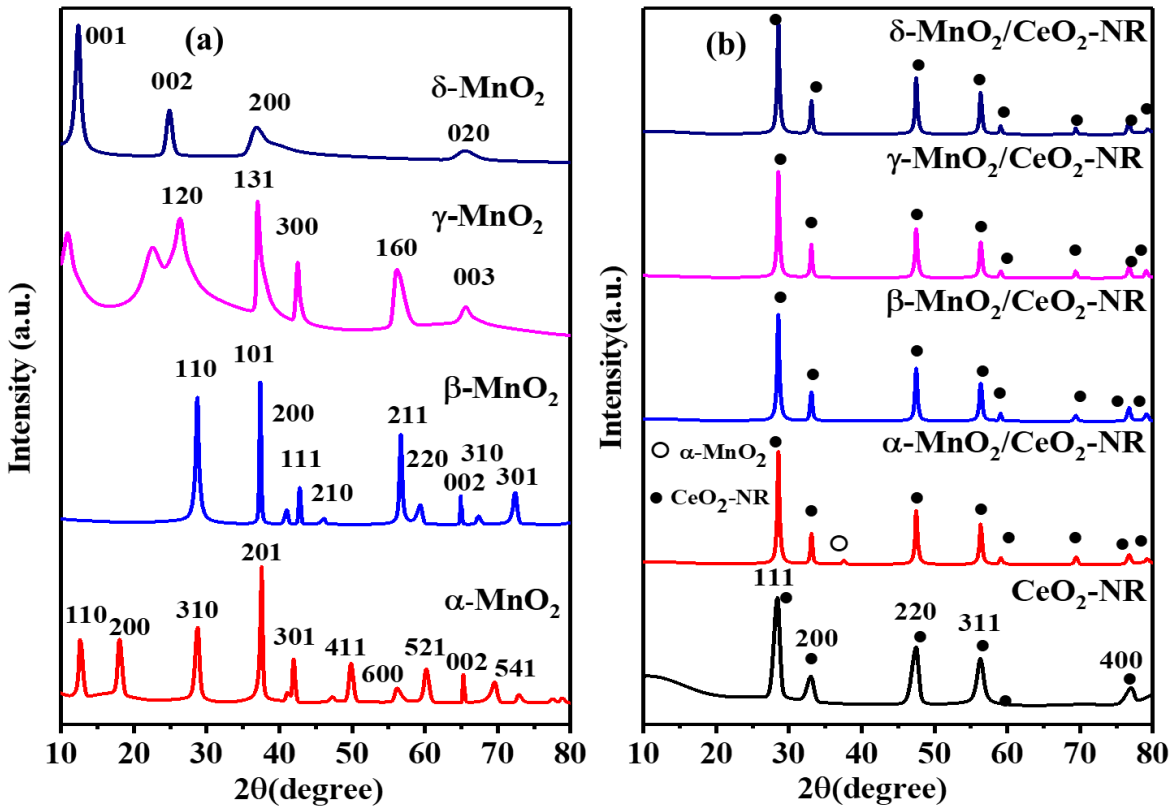

Fig. 6.2. XRD of (a) active metals and (b) catalysts

CeO_2-NR (JCPDS 98-010-8718, cubic, a=5.4120Å) and for catalysts (JCPDS 98-010-8718, cubic, a=5.4120Å), the reflection peaks are observed at 2θ values of 28.84°, 33.27°, 47.68°, 56.66°, 59.31°, 69.69°, 76.89°, 79.29°, and 88.52° corresponded to (111), (200), (220), (311), (400), (331), (420), and (422) planes respectively, shown in **Fig. 6.2(b)**. After impregnation of β-MnO_2, δ-MnO_2, and γ-MnO_2 on CeO_2-NR supports, no extra peaks were observed, and only a single small peak was observed in α-MnO_2/CeO_2-NR catalyst for α-MnO_2, which shows that the metals are well dispersed on the ceria support. [8,9] **Table 6.2** shows the average crystal sizes of the samples, which were calculated using the Scherrer formulation from the half-peak width of the diffraction peak. The crystal size of α-MnO_2/CeO_2-NR is the lowest (15.22 nm), and the crystal size of β-MnO_2/CeO_2-NR is the highest (21.25 nm).

Table 6.2. The average crystal size, lattice parameters, and particle size of the samples

Sample	Average crystal size (nm)[a]	Average particle size (nm)[b]	Lattice parameter (Å)	Lattice strain ((Δd/d) [c]
CeO_2-NR	12.90	46.23	5.412	0.0178
α-MnO_2/CeO_2-NR	15 .22	90.00	5.416	0.0367
β-MnO_2/CeO_2-NR	21.25	140.00	5.414	0.0298
γ-MnO_2/CeO_2-NR	12.21	110.00	5.410	0.0332
δ-MnO_2/CeO_2-NR	17.50	108.00	5.415	0.0339

[a] Scherrer equation, [b] *Particle size calculated from TEM image data*, [c] *Williamson-Hall method.*

6.2.3. X-ray Photoelectron Spectroscopy (XPS)

XPS was employed to determine the chemical state and surface composition of different phases of MnO_2 loaded on CeO_2-NR catalysts. The XPS spectrum of Ce 3 d, O1s and Mn 2p is shown in **Fig. 6.3**, and **Fig. 6.4**.

The Ce 3d XPS spectrum of catalysts is shown in **Fig. 6.3**. The Ce 3d spectra have two sets of spin-orbit lines, corresponding to Ce $3d_{3/2}$ and Ce $3d_{5/2}$ which represent u and v. The synthesized catalysts, which have cerium oxide, contain both tri-valent and the tetra-valent cerium ions. The de-convoluted split peaks confirm the existence of Ce^{3+} and Ce^{4+} ions in cerium di-oxides. The peaks u^0 and v^0 represent the Ce^{3+} species, while the other peaks v^i, v^{ii}, u^i, and u^{ii}, represent the Ce^{4+} species. [10] The proportion of oxygen in the lattice and the surface ion content of Ce^{3+} are critical factors in the performance of the materials. Since the presence of Ce^{3+} species may be used to semi-quantitatively determine the surface oxygen vacancy, the generation of surface oxygen vacancy from the removal of lattice oxygen species in CeO_2 resulted in the formation of Ce^{3+} species. The ratio of $Ce^{3+}/(Ce^{3+}+Ce^{4+})$ content of each catalyst was

calculated and is shown in **Table 6.4**. The α-MnO_2/CeO_2-NR catalyst exhibits the highest value among all catalysts which means the formation of more oxygen vacancies. [11]

Fig. 6.4(a) shows the XPS spectra of O1s where the peaks at higher binding energy (530.61 eV) are labelled for the surface adsorbed oxygen species (indicated as O_α), and the peaks at lower binding energy (528.8 eV) marked for the surface lattice oxygen species (indicated as O_β). [12,13] It is well known that surface chemisorbed oxygen O_α is important in reduction reactions due to its higher mobility than O_β. It provides acidic sites at the surface of the catalysts to adsorb NH_3 to form NH^{4+} (ads). [14] Therefore, the concentration ratios of $O_\alpha/(O_\alpha+O_\beta)$ were calculated and is shown in **Table 6.4**. The ratio is in the order of: α-MnO_2/CeO_2-NR (40.31%) > δ-MnO_2/CeO_2-NR (38.71%) > γ-MnO_2/CeO_2-NR (38.57%) > β-MnO_2/CeO_2-NR (36.25%) respectively. The α-MnO_2/CeO_2-NR catalysts possess the highest adsorbed oxygen species.

The Mn 2p spectra of the catalysts are shown in **Fig. 6.4(b)**, where two main peaks composed of Mn $2p_{1/2}$ and Mn $2p_{3/2}$ were observed. The Mn $2p_{3/2}$ and Mn $2p_{1/2}$ peaks at 642.1 eV and 654.2 eV binding energy corresponded to Mn^{4+} and Mn^{3+}, respectively, representing that the Mn was in the mixed-valence state (Mn^{4+} and Mn^{3+}). [15] As seen from the **Table 6.4**, the value of Mn^{4+}/ (Mn^{4+} + Mn^{3+}) is highest for α-MnO_2/CeO_2-NR (72.56%) followed by δ-MnO_2/CeO_2-NR (72.23%), γ-MnO_2/CeO_2-NR (70.01%) and β-MnO_2/CeO_2-NR (67.11%). According to the literature, Mn^{4+} species has higher redox capacity than Mn^{3+}, which is preferable for low-temperature NH_3-SCR reaction. [16]

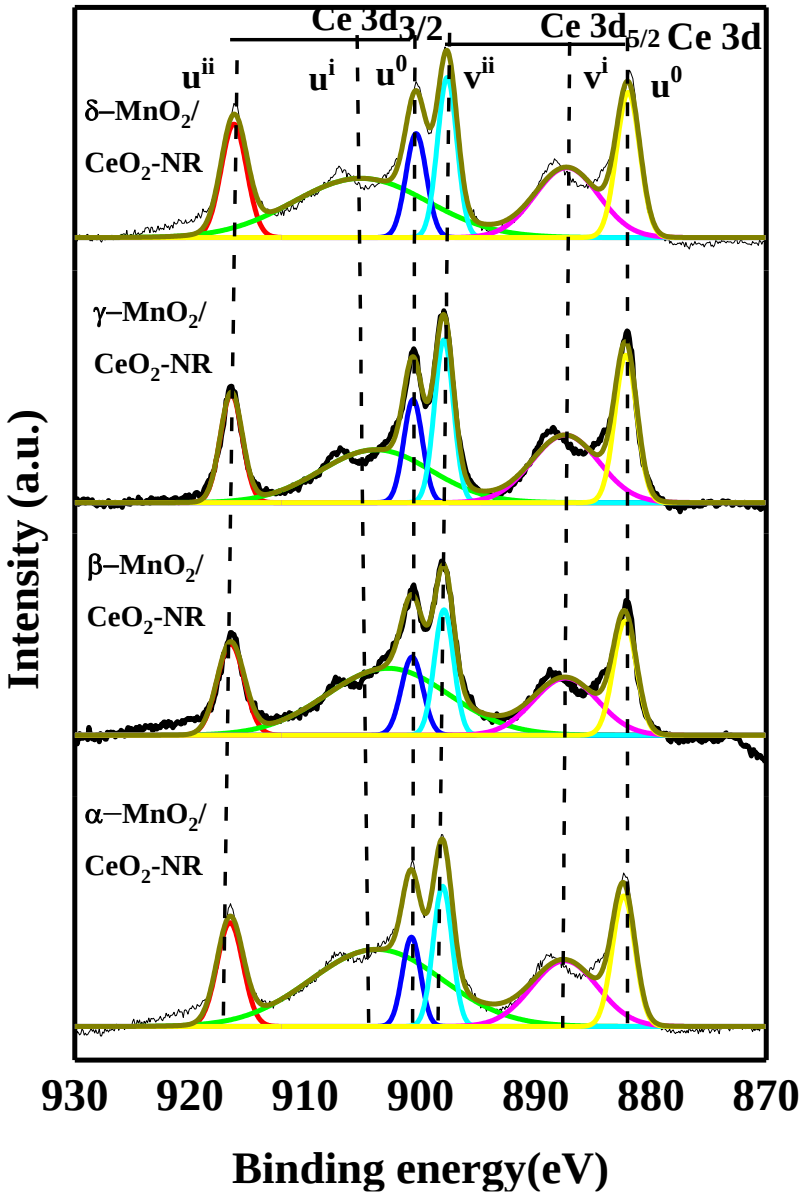

Fig. 6.3. Ce 3d XPS spectra of the catalysts

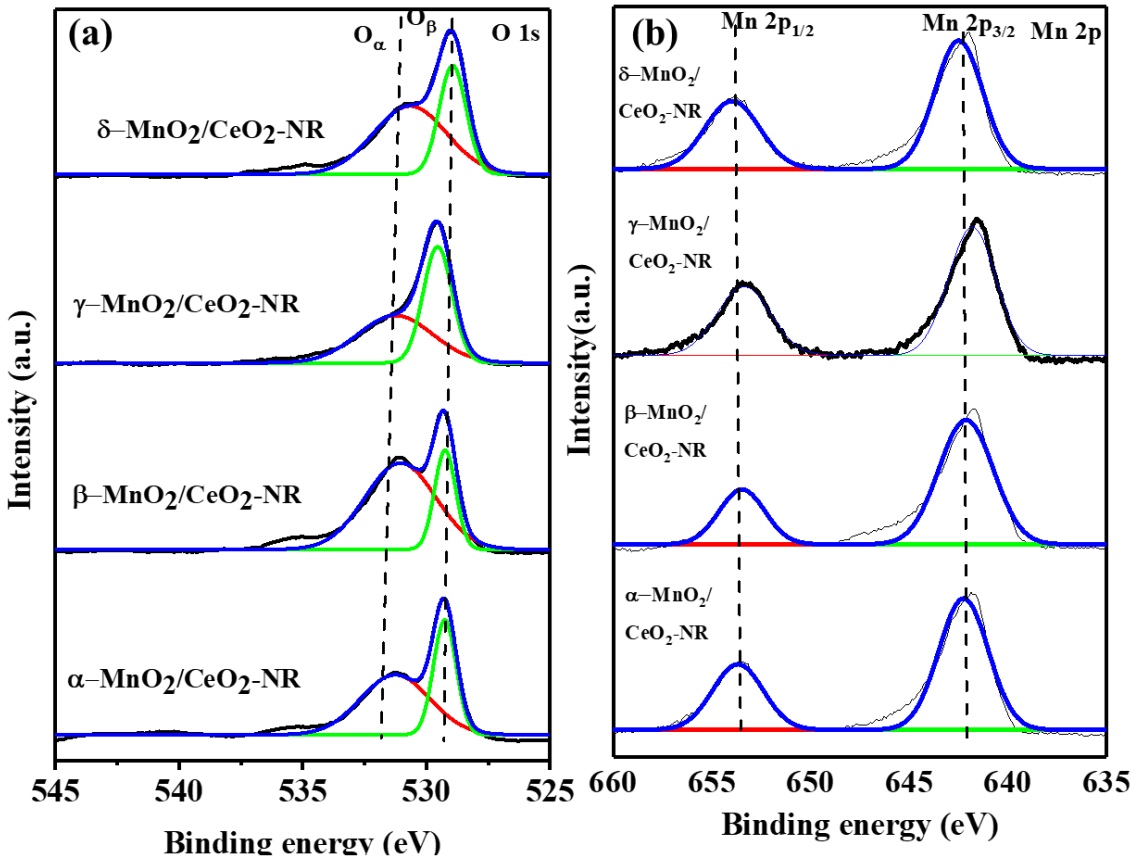

Fig. 6.4. XPS spectra of (a) O 1s and (b) Mn 2p of the catalysts

Table 6.3. XPS results of O 1s and Mn 2p of the catalysts

Sample	Mn^{4+}	Mn^{3+}	O_α	O_β
	Be (eV)	Be (eV)	Be (eV)	Be (eV)
α-MnO_2/CeO_2-NR	642.12	653.63	531.22	529.34
β-MnO_2/CeO_2-NR	642.29	653.46	531.02	529.21
γ-MnO_2/CeO_2-NR	641.77	653.29	531.42	529.61
δ-MnO_2/CeO_2-NR	642.54	653.96	530.68	529.01

Table 6.4. XPS results of O 1s, Ce 3d, and Mn 2p of the catalysts

Sample	Surface atomic concentration (%)		
	$(\frac{O_\alpha}{O_\alpha+O_\beta})\%$	$(\frac{Ce^{3+}}{Ce^{3+}+Ce^{4+}})\%$	$(\frac{Mn^{4+}}{Mn^{4+}+Mn^{3+}})\%$
α-MnO_2/CeO_2-NR	40.31	39.23	72.56
β-MnO_2/CeO_2-NR	36.25	37.11	67.11
γ-MnO_2/CeO_2-NR	38.57	37.50	70.01
δ-MnO_2/CeO_2-NR	38.71	38.03	71.73

6.2.4. Scanning Electron Microscopy- Energy Dispersive X-ray Spectroscopy (SEM-EDX)

The SEM examination was carried out to anaylzed surface morphology. At the same time, the EDX and elemental mapping were used to identify the elemental composition of materials and to determine the active metal distribution on the support surface and results are shown in **Fig.6.5** and **Fig.6.6**, respectively. **Fig.6.5** shows the SEM-EDX images of CeO_2-NR supports, while the **Fig.6.5(b-e)** shows the SEM-EDX images of α-MnO_2/CeO_2-NR β-MnO_2/CeO_2-NR, γ-MnO_2/CeO_2-NR, and δ-MnO_2/CeO_2-NR catalysts, respectively. The SEM image of CeO_2-NR shows large particles and material accumulation on the surface materials. After the impregnation of the active metals on ceria support, it was observed that the surface of the catalysts was changed to smooth. Further accumulation can be observed in the images of β-MnO_2/CeO_2-NR and γ-MnO_2/CeO_2-NR catalysts. The SEM images of α-MnO_2/CeO_2-NR and δ-MnO_2/CeO_2-NR catalyst surface shows homogeneous distribution of the materials on the surface and small particle size compared to all three other catalysts. The elemental composition of synthesized CeO_2-NR support and catalysts was investigated using EDX. The presence of Ce and O in the synthesized support was effectively confirmed by EDX results for CeO_2-NR

(**Fig.6.5(a)**). The presence of Ce, Mn, and O was observed in the EDX spectra of all the catalyst materials confirming the metal dispersion (**Fig. 6.5(b)**, **(c)**, **(d)**, and **(e)**). A small fraction of the sample was used for the elemental analysis stated in the EDX analysis, which assumed the sample had a uniform composition. Furthermore, the elemental mapping also confirmed the presence of all desired elements, distributed homogeneously in all the samples, as shown in **Fig.6.6**.

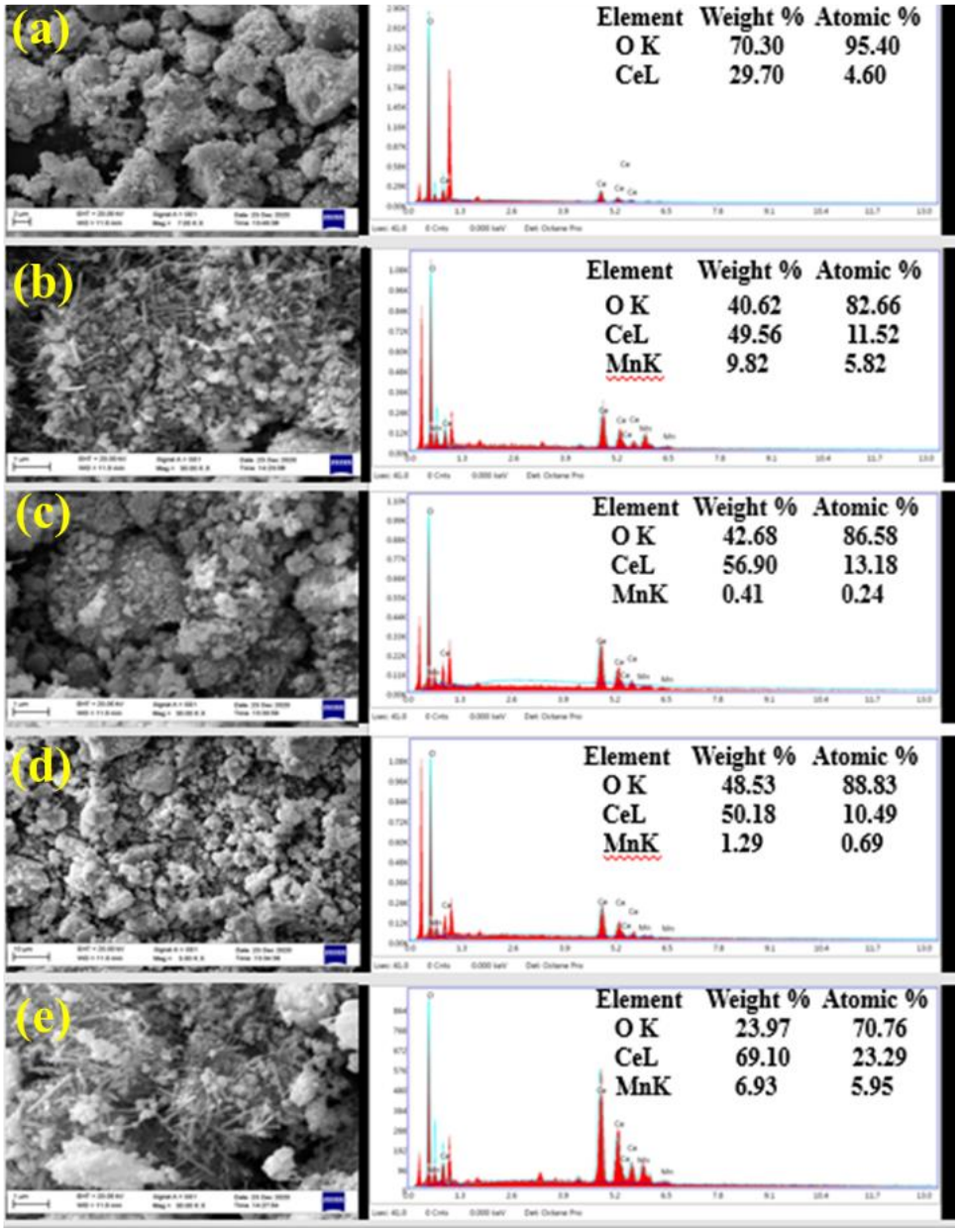

Fig. 6.5. SEM-EDX images of (a) CeO_2-NR, (b) α-MnO_2/CeO_2-NR (c) β-MnO_2/CeO_2-NR (d) γ-MnO_2/CeO_2-NR, and (e) δ-MnO_2/CeO_2-NR

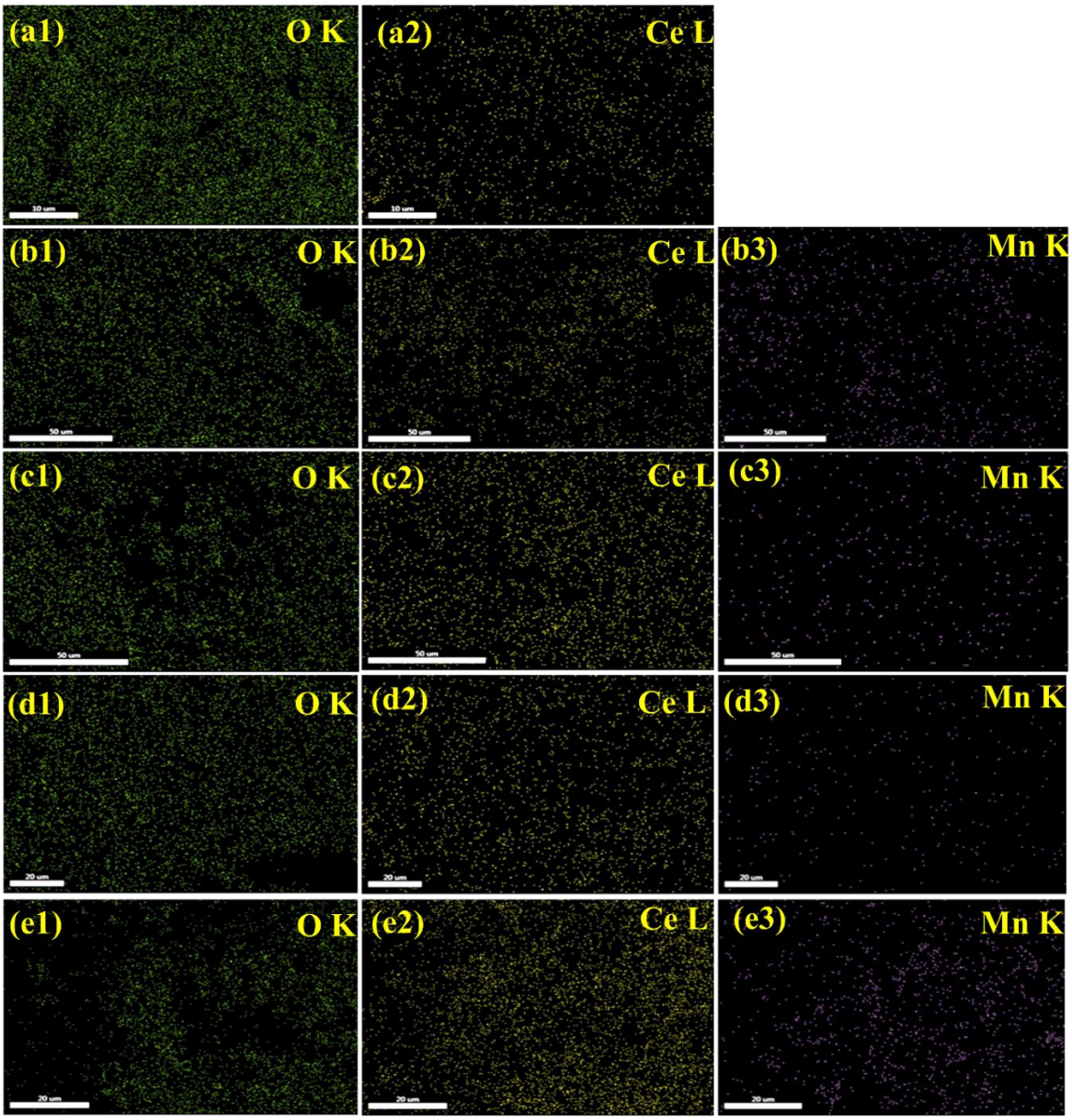

Fig. 6.6. Elemental mapping of CeO_2-NR [(a1), (a2)], α-MnO_2/CeO_2-NR [(b1), (b2), (b3)] β-MnO_2/CeO_2-NR [(c1), (c2), (c3))], γ-MnO_2/CeO_2-NR [(d1), (d2), (d3)], and δ-MnO_2/CeO_2-NR [(e1), (e2), (e3)]

6.2.5. Transmission Electron Microscopy (TEM)

TEM was applied to obtain information about the morphologies of the different crystal phases of MnO_2 which shown in **Fig.6.7**. The morphologies for CeO_2-NR are withstood after the α-MnO_2, β-MnO_2, γ-MnO_2, and δ-MnO_2 are impregnated. The EDX data (**Fig. 6.5**) also

confirmed the active metals present on the surface of the CeO_2-NR in the catalysts. The average particle size of the samples is shown in **Table 6.2**, in which the α-MnO_2/CeO_2-NR (90 nm) shows the smallest average particle size, followed by the δ-MnO_2/CeO_2-NR (108 nm), γ-MnO_2/CeO_2-NR (110 nm), and β-MnO_2/CeO_2-NR (140 nm), respectively. The particle size of catalysts increased after metal impregnation, followed by the same series as the average crystal size of the catalysts in **Table 6.2**. The SAED consists of the observation of the pattern of diffraction spots obtained on the TEM viewing screen from a randomly oriented particle. Such a pattern indicates that the material is crystalline, which is also confirmed by the XRD (**Fig. 6.2**).

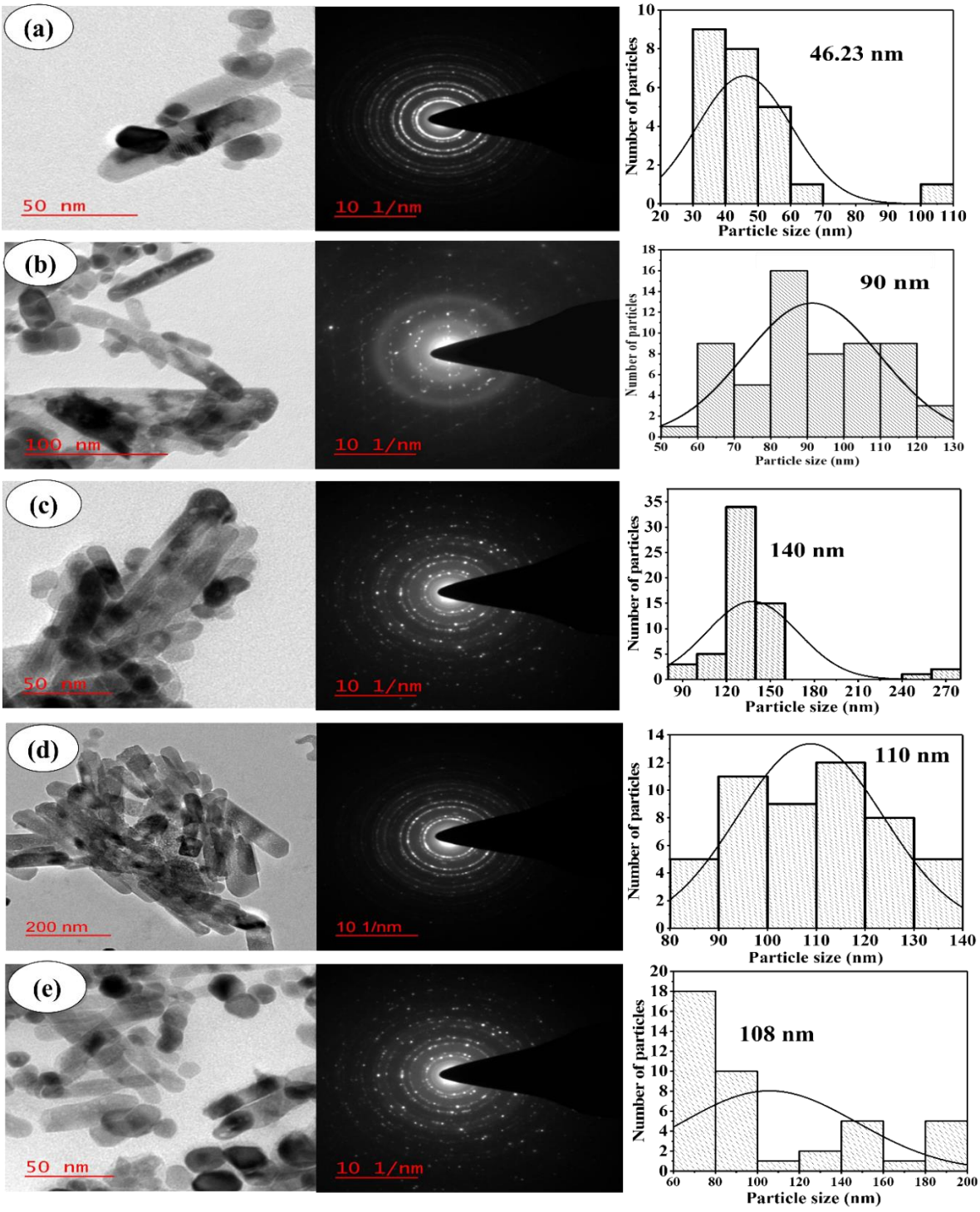

Fig. 6.7. TEM images of (a) CeO_2-NR, (b) α-MnO_2/CeO_2-NR, (c) β-MnO_2/CeO_2-NR, (d) γ-MnO_2/CeO_2-NR, and (e) δ-MnO_2/CeO_2-NR catalysts

6.2.6. Raman Spectroscopy

The CeO_2-NR and catalyst structures were further characterized using Raman spectroscopy, which is shown in **Fig.6.8**. According to Raman spectra, CeO_2-NR exhibited a strong Raman band at 465 cm^{-1} and a shoulder at 600 cm^{-1}, attributed to the F_{2g} vibration and defect-induced modes (D band), respectively, of the cubic fluorite structure. [17,18] For ceria-based materials, the oxygen vacancy concentration is shown by the area ratio of D and F_{2g} (A_D/A_{F2g}), which is associated with the D band in ceria-based materials. [19,20] As shown in **Fig.6.8**, the MnO_x/CeO_2-NR catalysts also showed the F2g vibration mode and defect-induced mode (D band) of CeO_2-NR. Due to the electronic interactions between MnO_x and CeO_2-NR, the F2g peak broadens and shifts to the lower wavenumber following the impregnation of active metals on CeO_2-NR supports. [21] Thus, according to **Fig.6.8**, the F2g bands of the catalysts α-MnO_2/CeO_2-NR, β-MnO_2/CeO_2-NR, γ-MnO_2/CeO_2-NR, and δ-MnO_2/CeO_2-NR shifted to 449, 448, 449, and 447 cm^{-1}, respectively. Parallel to this shift, the D band was also improved. In addition, Mn species were incorporated into the CeO_2 lattice to generate a homogeneous ceria-based solid solution (containing Mn-O-Ce structures). A defect in the surface of CeO_2 resulted from enhanced lattice perturbations and structural strain induced by substituting Mn^{n+} with Ce^{4+} (such as Mn^{4+} and Mn^{3+}) (e.g., oxygen vacancies). Enhanced oxygen migration enhanced NO oxidation to NO_2 and NH_3-SCR catalytic performance. [22] **Fig.6.9** summarizes the oxygen vacancy concentrations (A_D/A_{F2g}) for these MnO_x/CeO_2 catalysts**.** The order is in this order: α-MnO_2/CeO_2-NR (0.361) > δ-MnO_2/CeO_2-NR (0.218) > γ-MnO_2/CeO_2-NR (0.057) > β-MnO_2/CeO_2-NR (0.042) > CeO_2-NR (0.034). Due to the incorporation of Mn^{n+} into the CeO_2 lattice, the α-MnO_2/CeO_2-NR catalyst showed the highest oxygen vacancy proportion of all synthesized samples (confirmed by XPS). The high temperatures and high pressures during hydrothermal treatment resulted in a uniform ceria-related solid solution (containing Mn-O-Ce), which enhanced the electronic interactions between MnO_x and CeO_2.

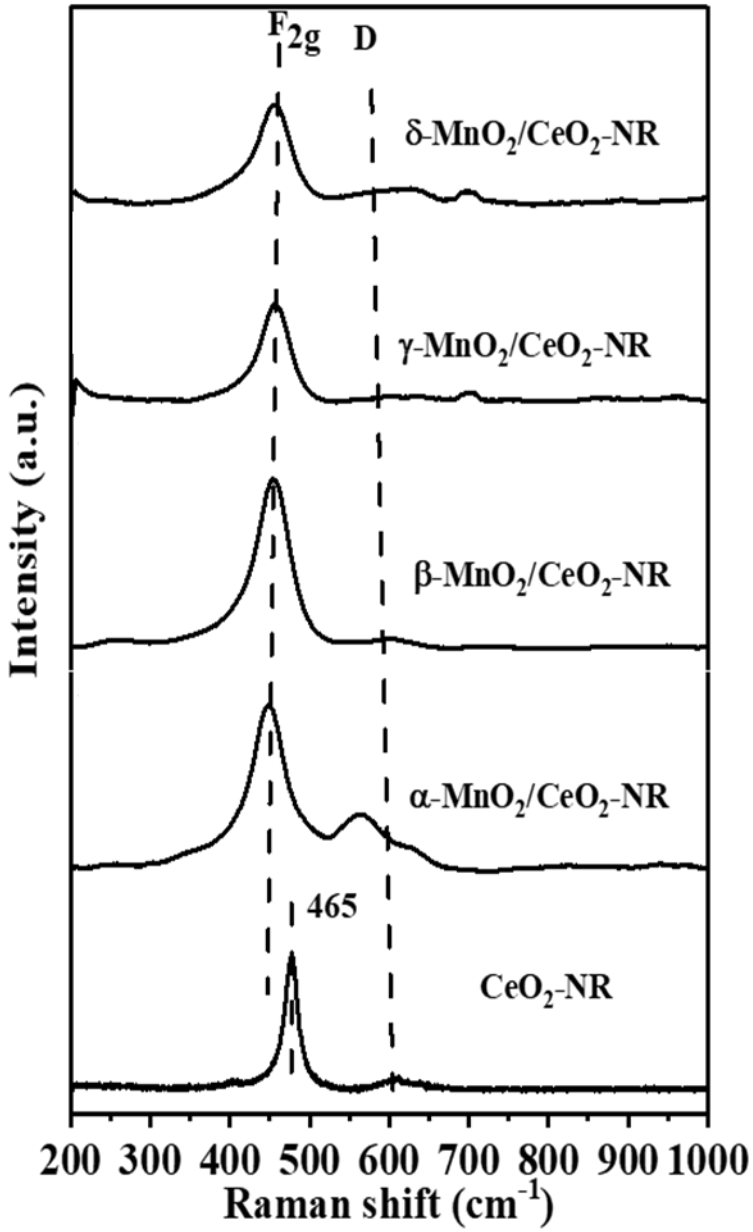

Fig. 6.8. Raman analysis of the support and catalysts

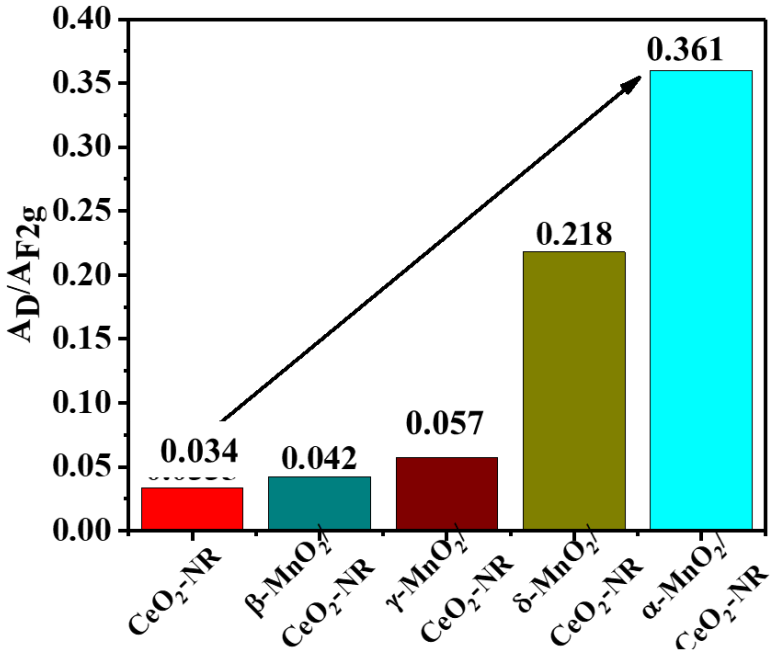

Fig. 6.9. A_D/A_{F2g} data of the support and catalysts

6.2.7. Activity Measurements

3.2.7.1. Effects of temperature on different Phase of MnO_2 catalysts

The catalytic activities of different phases of MnO_2 loaded on ceria support were tested in the temperature range of 50–450°C. The NO conversion and N_2 selectivity as a function of temperature is shown in **Fig.6.10**. The NO conversion is highest (61%) at 350°C for the MnO_2/CeO_2-NR catalyst. NO conversions of α-MnO_2/CeO_2-NR and δ-MnO_2/CeO_2-NR increased rapidly with the increasing temperature between 50 and 250 °C and reached their maximum conversion at 250 °C, afterward showed a slight decrease until 300 °C, followed by a rapid decrease afterward. At the same time, β-MnO_2/CeO_2-NR and γ-MnO_2/CeO_2-NR showed slight variation (**Fig.6.10(a)**). The graph clearly shows that the three catalysts' NO conversion rates over the specified temperature range were as follows: α-MnO_2/CeO_2-NR > δ-MnO_2/CeO_2-NR > γ-MnO_2/CeO_2-NR > β-MnO_2/CeO_2-NR, this result is in accordance with the BET surface area results, which show that an increase in surface area is favourable to NH_3-SCR. [23] As shown in **Fig.6.10(a)**, the α-MnO_2/CeO_2-NR exhibits the maximum NO

conversion. When the temperature reached 250 °C, 75% NO conversion and 86% N_2 selectivity were attained, as shown in **Fig.6.10(b)**. The NO conversion for the other three catalysts, β-MnO_2/CeO_2-NR, γ-MnO_2/CeO_2-NR, and δ-MnO_2/CeO_2-NR, is 45, 61, and 69%, respectively. The N_2 selectivity for the other three catalysts is between 79 and 84%. The different phases of catalysts (α-MnO_2/CeO_2-NR, β-MnO_2/CeO_2-NR, γ-MnO_2/CeO_2-NR, δ-MnO_2/CeO_2-NR) shifted to lower temperature compared to the MnO_2/CeO_2-NR.

The α-MnO_2/CeO_2-NR catalysts show the highest surface area, highest pore volume, and largest diameter compared to all three other catalysts, as shown in **Table 6.1**, resulting in the highest active surfaces and the most effective interactions between reactant and catalyst. The Raman also show good interaction between active metals and ceria supports for α-MnO_2/CeO_2-NR catalyst. Mn is dispersed uniformly and provides more roughness, forming more active sites, as confirmed by BET and SEM-EDX analysis. Additionally, compared to the other three catalysts, the α-MnO_2/CeO_2-NR catalyst possesses the highest surface concentrations of the Ce^{3+} (39.23%) and Mn^{4+} (72.56%) species. Also, it contains a higher surface oxygen vacancy (40.31%), which enhances the activity and is crucial in reduction reactions due to its mobility. [24,25] These are the reasons behind the better performance of the α-MnO_2/CeO_2-NR catalyst than that of other catalysts. **Fig.6.11** illustrates the connection between surface lattice defects, surface oxygen, and reaction rates. Both graphs, **Fig.6.11(a)** and **Fig.6.11(b)** reveal that an increase in the catalyst's A_D/A_{F2g} and O_α leads to an increased reaction rate, consequently increasing NO conversion. This observed relationship is further validated by the NO conversion graph, highlighting the pivotal role of surface lattice defects and oxygen content in influencing the overall catalytic performance and emissions of nitrogen oxides (NO).

To reduce the external mass transfer and internal diffusion, the kinetic investigation was conducted at low NO conversion (below 25%). For all catalysts, the catalytic performance was satisfactory. According to the Arrhenius equation, all catalysts had significant activation energies with values between 21 and 65 KJ.mol^{-1}, as shown in **Fig.6.12(a)**. But out of all, the α-MnO_2/CeO_2-NR catalyst showed the lowest activation energy, in line with the NO conversion data, which shows that the α-MnO_2/CeO_2-NR gave the highest performance. [26,27]

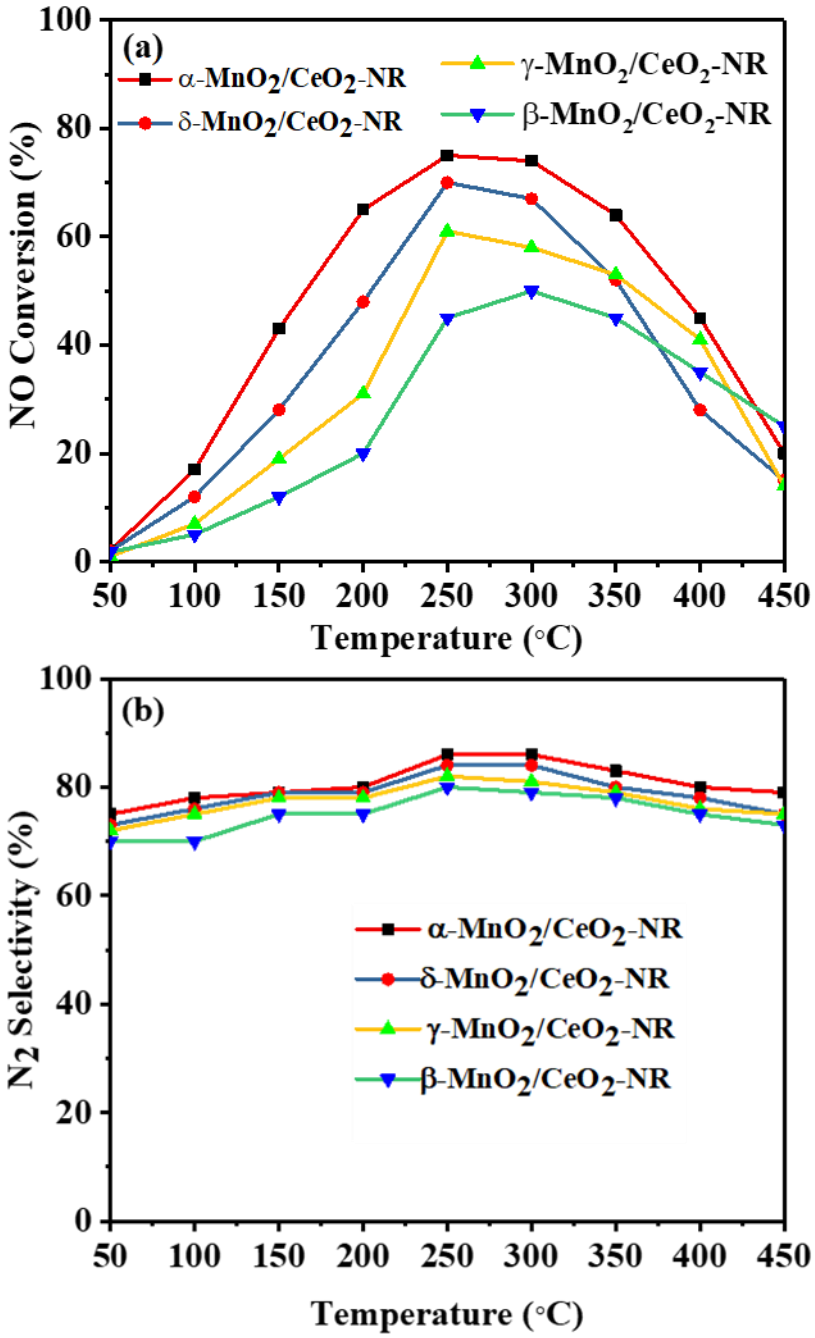

Fig. 6.10. Effects of temperature on (a) NO conversions, and (b) N_2 selectivity

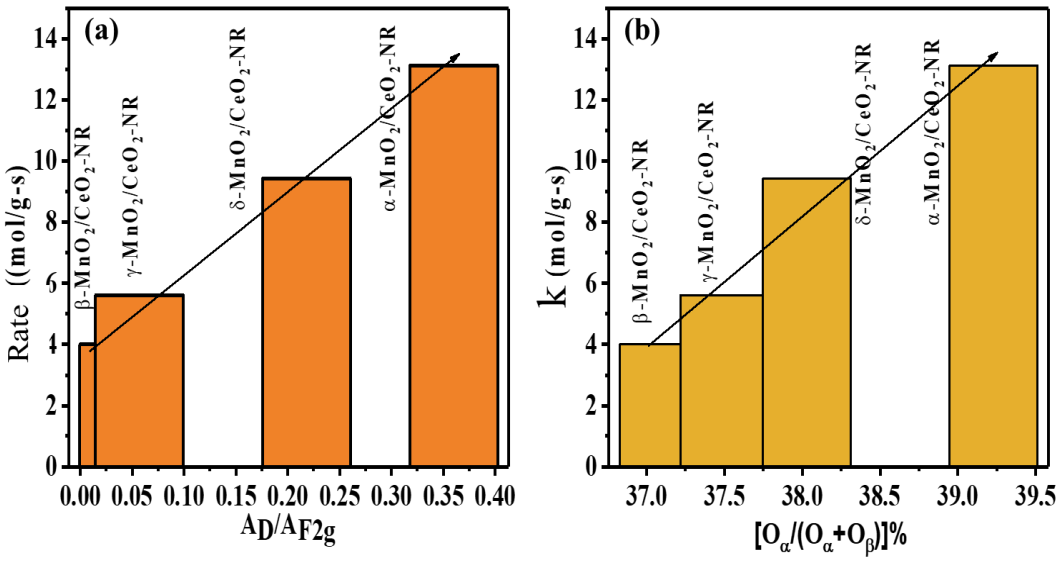

Fig. 6.11. Effect of (a) surface lattice defects and (b) surface oxygen on reaction rate

6.2.7.2. Catalytic stability test

The effectiveness of the NH_3-SCR catalysts on practical scale can be evaluated using the catalyst's long-term stability**.** The stability test lasting 25 h was conducted at 250°C, as shown in **Fig.6.12(b)**. The NO conversion of α-MnO_2/CeO_2-NR catalyst stays close to 75%, and the selectivity of N_2 to 86% remains relatively steady throughout the 25-h continuous procedure with a slight fluctuation of around ±1% over time. The α-MnO_2/CeO_2-NR catalyst behaves extremely steadily throughout 25 h at 250 °C, as can be seen by the almost complete absence of any deactivation.

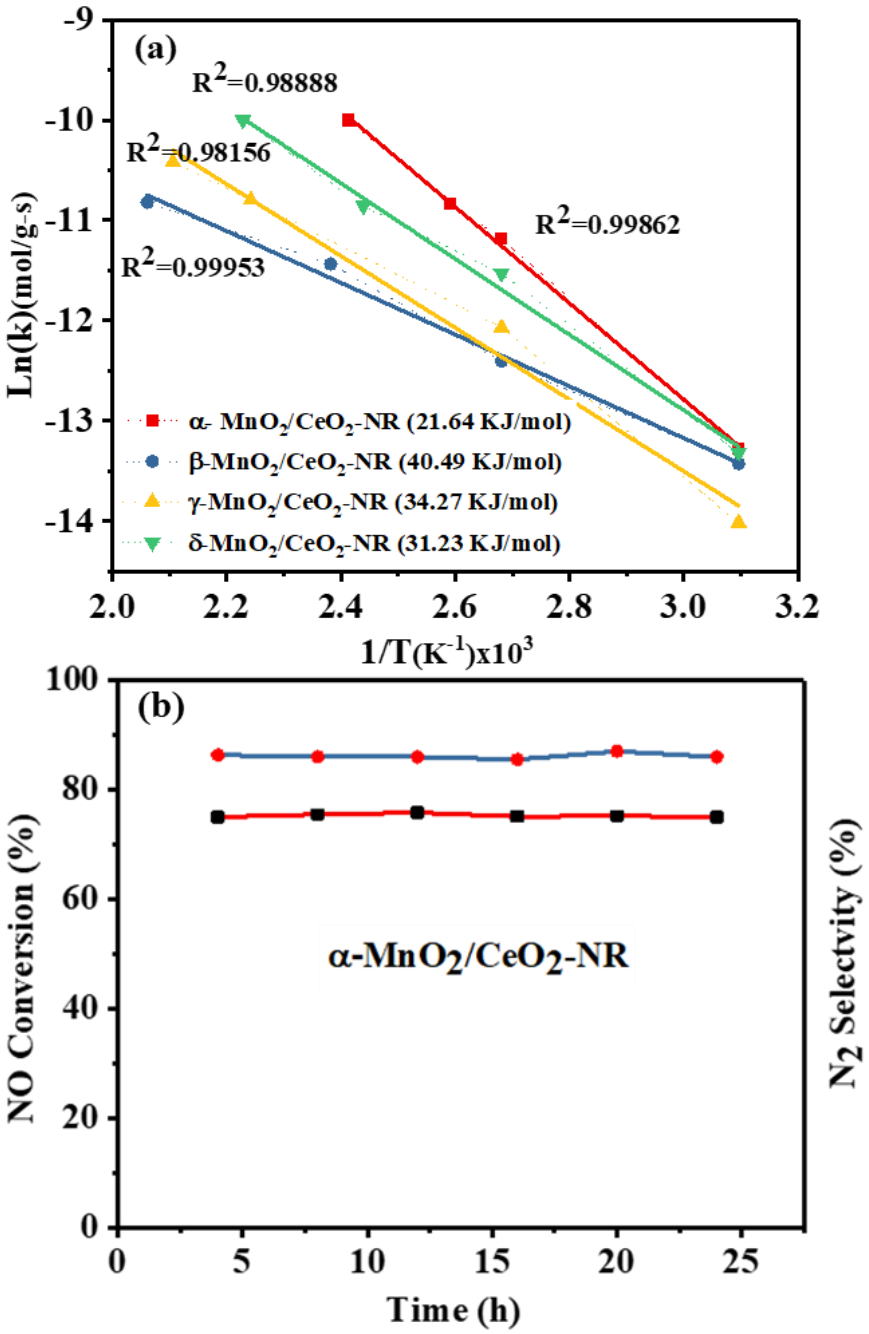

Fig. 6.12. (a) Activation energy of the catalysts, and (b) Catalytic stability test on α-MnO_2/CeO_2-NR catalyst

6.2.7.3. Effects of temperature on α-MnO_2 loading

The influence of α-MnO_2 loading amount on CeO_2/NR catalyst activity was investigated with different wt.% of α-MnO_2 (5, 8, 11, 13, and 17 wt.%). The results are given in **Fig.6.13**. The

reaction conditions were: 0.4 gm catalyst, temperature range 50–450 °C, NO and NH_3 =1000 ppm, O_2 = 6 vol%, Ar balance, and GHSV =13,000 h^{-1}. From the graph in **Fig.6.13(a)**, NO conversion also increases when the amounts of wt.% of α-MnO_2 increase from 5 to 14%. This indicates that Mn's presence increases the overall number of active sites present in the catalysts. In general, the increase in the number of active sites in the catalyst has enhanced the catalytic activity of the catalyst. [26,28] However, NO conversion is constant when α-MnO_2 loading amounts change from 14 to 17%, which may be due to the aggregation of the active metal. All the experimental results indicate that SCR catalysts show optimal performance when the α-MnO_2 loading amount reaches 14% and NO conversion arrives at 94.25% at a reaction temperature of 250 °C. As seen in **Fig.6.13**, the SCR catalyst shows the highest activity at 250 °C, indicating that the SCR catalyst is suitable for NO reduction at low temperatures. NO conversion reaches its maximum with an α-MnO_2 loading amount of 14%, and the N_2 selectivity is more than 95%. When the loading is between 14 and 17 wt.%, unfavourable synergism between α-MnO_2 and CeO_2-NR, the high agglomeration or cluster formation of α-MnO_2, and the reduction of the active surface area, may be the factors for its low activity. On the other hand, the 14-17 wt.% α-MnO_2/CeO_2-NR exhibits a higher N_2 selectivity than the 5 and 11 wt.% α-MnO_2 loading over CeO_2-NR. The N_2 selectivity may depend on other physicochemical properties of catalysts, such as Ce^{3+} and surface oxygen, and not on the catalyst's surface area or pore volume; that is why it is not affected after increasing the α-MnO_2 loading.

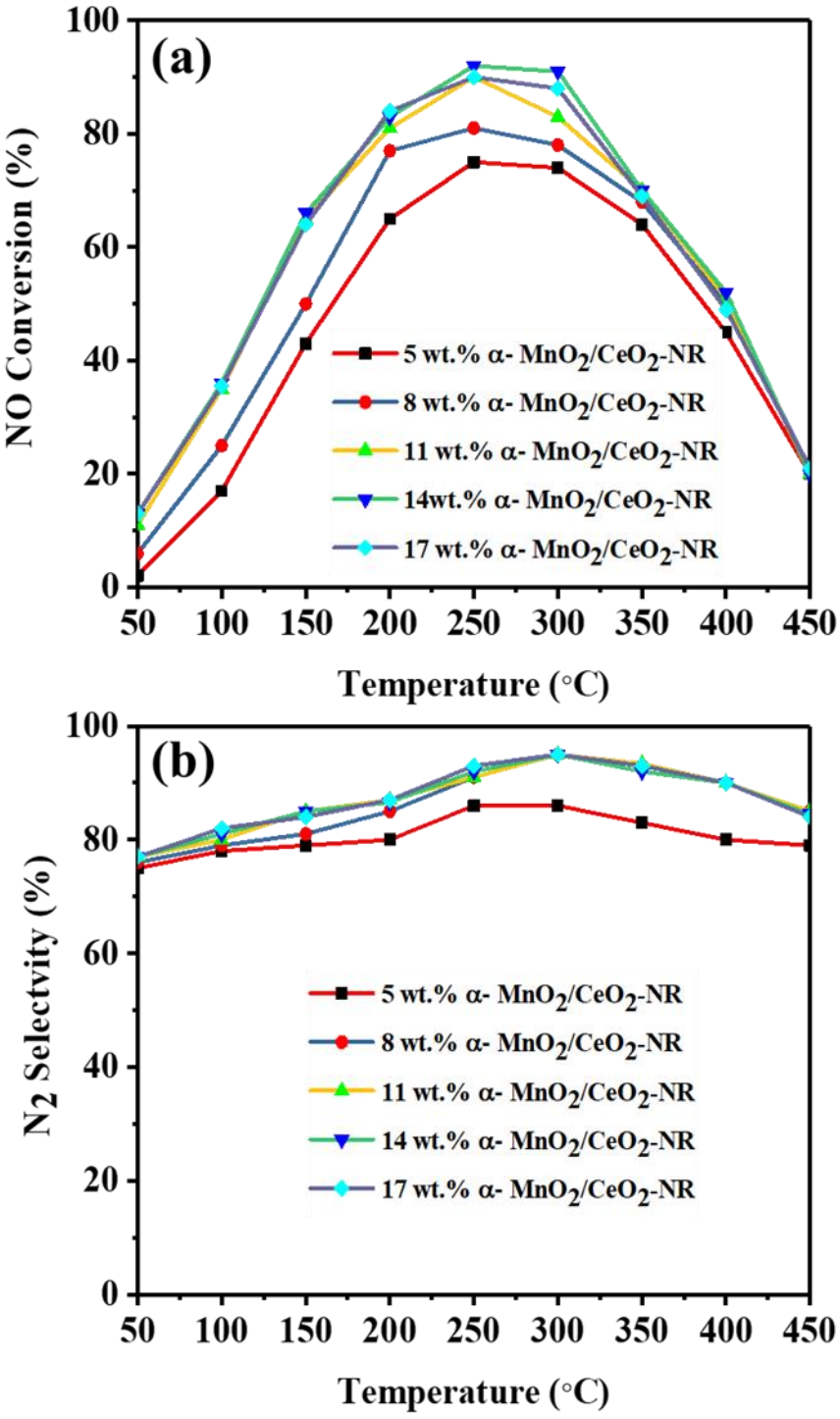

Fig. 6.13. Effects of α-MnO_2 loading on (a) NO conversions and (b) N_2 selectivity

6.2.7.4. Characterization of spent catalysts

Fig.6.14 depicts the X-ray diffraction patterns of the spent catalysts. As shown in the **Fig.5.14**, no significant alterations were observed in the diffraction patterns the peaks appeared sharper.

As indicated in **Table 6.5**, there was an increase in the crystal size of the catalysts, which is likely due to cluster formation at high temperatures.

The TEM images of the spent catalysts are shown in **Fig.6.15**. In comparison to **Fig.6.7;** the morphology properties of the spent catalysts remained unchanged despite exposure to high temperatures. However, certain catalysts displayed larger particles, possibly attributed to clustering.

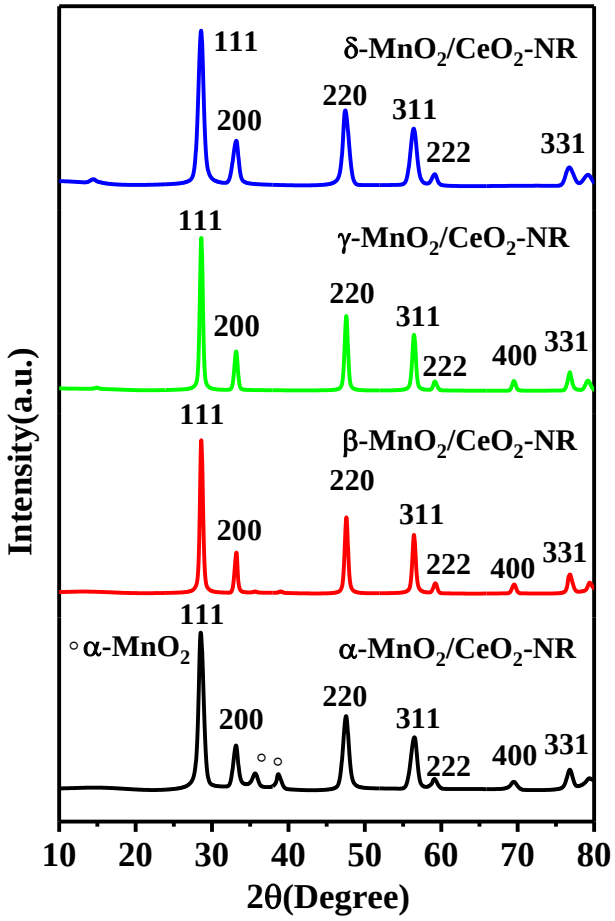

Fig. 6.14. XRD of spent α-MnO_2/CeO_2-NR, β-MnO_2/CeO_2-NR, γ-MnO_2/CeO_2-NR and δ-MnO_2/CeO_2-NR catalysts

Table 6.5. Average crystal size and particle size of the spent catalysts

Catalyst	Average crystal size (nm)	Average particle size (nm)
α-MnO_2/CeO_2−NR	16.21	91
β-MnO_2/CeO_2−NR	22.98	145
γ-MnO_2/CeO_2−NR	14.76	108
δ-MnO_2/CeO_2−NR	19.21	114

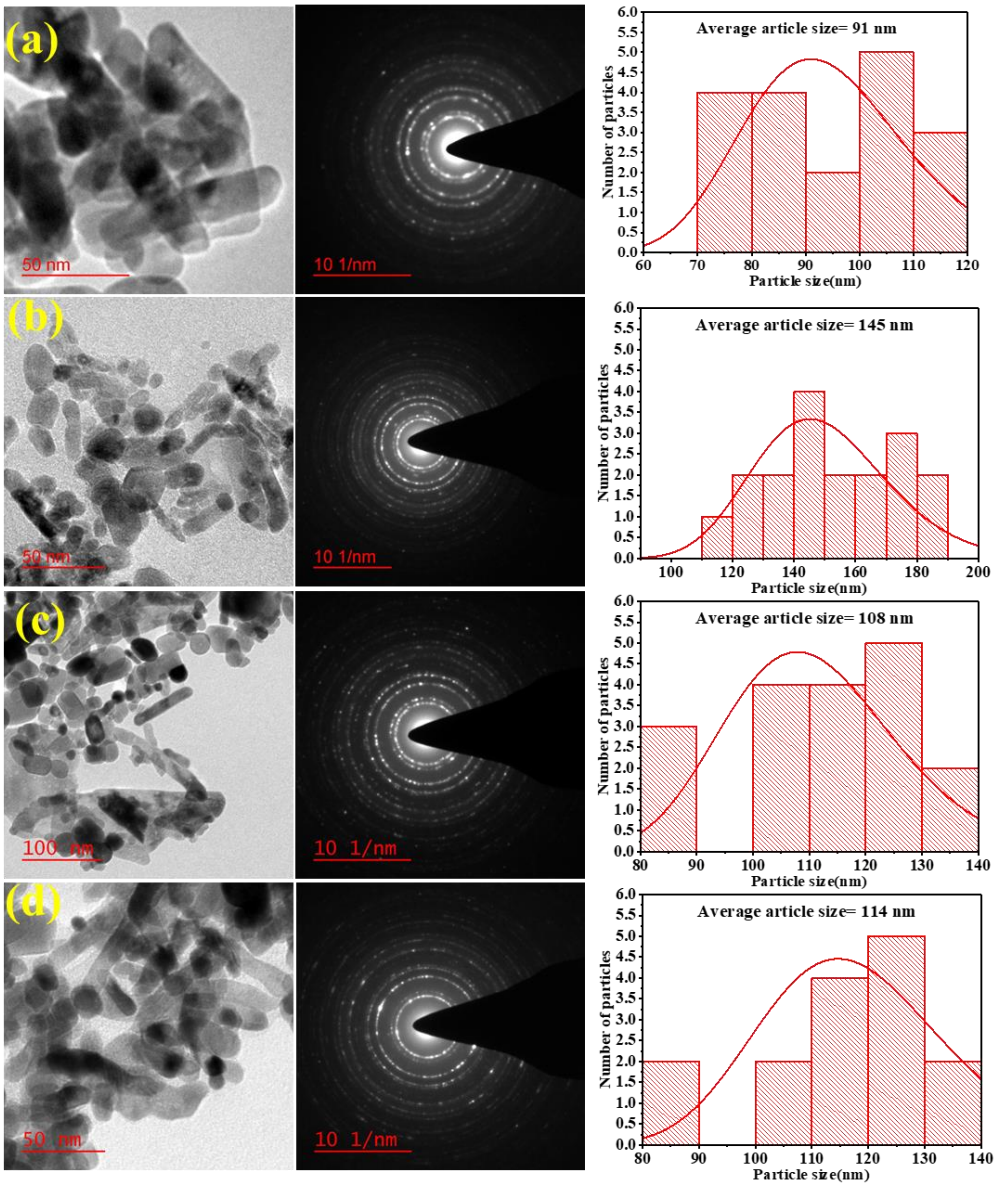

Fig. 6.15. TEM images of (a) spent MnO_2/CeO_2-NR, (b) spent Mn_2O_3/CeO_2-NR, and (c) spent MnO/CeO_2-NR catalysts

6.3. Conclusions

The different phase structures (α, β, γ, and δ) of MnO_2 were synthesized through the hydrothermal method and impregnated on CeO_2-NR support through the wet-impregnation process. The prepared catalysts were investigated for NO reduction through the SCR method using NH_3 as a reducing agent. The results showed that the NO conversion decreased in the following order: α-MnO_2/CeO_2-NR < δ-MnO_2/CeO_2-NR < γ-MnO_2/CeO_2-NR < β-MnO_2/CeO_2-NR in the 50-450°C temperature range. The α-MnO_2/CeO_2-NR catalysts showed the highest 75% NO conversion and 86% N_2 selectivity, and it remained stable with a slight fluctuation around ±1% after undergoing a 25-h catalytic stability test. Characterization analysis through BET, XRD, XPS, TEM, SEM-EDX, and Raman spectroscopy showed that the specific surface area, surface Ce^{3+} and Mn^{4+}, and oxygen storage capacity were the significant properties governing the performances of the catalysts. The α-MnO_2/CeO_2-NR catalyst showed the highest activity due to all these favourable properties.

References

1. Park, Y.K. and Kim, B.S., 2023. Catalytic removal of nitrogen oxides (NO, NO_2, N_2O) from ammonia-fueled combustion exhaust: A review of applicable technologies. *Chemical Engineering Journal*, *461*, p.141958.
2. Kang, D., Bian, Y., Shi, Q., Wang, J., Yuan, P. and Shen, B., 2022. A Review of Synergistic Catalytic Removal of Nitrogen Oxides and Chlorobenzene from Waste Incinerators. *Catalysts*, *12*(11), p.1360.
3. Sun, M., Lan, B., Lin, T., Cheng, G., Ye, F., Yu, L., Cheng, X. and Zheng, X., 2013. Controlled synthesis of nanostructured manganese oxide: crystalline evolution and catalytic activities. *CrystEngComm*, *15*(35), pp.7010-7018.
4. Li, S., Zheng, Z., Zhao, Z., Wang, Y., Yao, Y., Liu, Y., Zhang, J. and Zhang, Z., 2022. CeO_2 Nanoparticle-Loaded MnO_2 Nanoflowers for Selective Catalytic Reduction of NO_x with NH_3 at Low Temperatures. *Molecules*, *27*(15), p.4863.
5. Wang, C., Yu, F., Zhu, M., Tang, C., Dong, L. and Dai, B., 2018. Synthesis of Both Powdered and Preformed MnO_x–CeO_2–Al_2O_3 Catalysts by Self-Propagating High-Temperature Synthesis for the Selective Catalytic Reduction of NO_x with NH_3. *ACS omega*, *3*(5), pp.5692-5703.
6. Huang, F., Ye, D., Guo, X., Zhan, W., Guo, Y., Wang, L., Wang, Y. and Guo, Y., 2020. Effect of ceria morphology on the performance of MnO_x/CeO_2 catalysts in catalytic combustion of N, N-dimethylformamide. *Catalysis Science & Technology*, *10*(8), pp.2473-2483.
7. Lian, Z., Shan, W., Zhang, Y., Wang, M. and He, H., 2018. Morphology-dependent catalytic performance of NbO_x/CeO_2 catalysts for selective catalytic reduction of NOx with NH_3. *Industrial & Engineering Chemistry Research*, *57*(38), pp.12736-12741.

8. Wang, D., Peng, Y., Yang, Q., Hu, F., Li, J. and Crittenden, J., 2019. NH_3-SCR performance of WO_3 blanketed CeO_2 with different morphology: Balance of surface reducibility and acidity. *Catalysis Today*, *332*, pp.42-48.
9. Gong, L., Liu, C., Liu, Q., Dai, R., Nie, X., Lu, L., Liu, G. and Hu, X., 2019. CuO/CeO_2–MnO_2 Catalyst Prepared by Redox Method for Preferential Oxidation of CO in H_2-Rich Gases. *Catalysis Surveys from Asia*, *23*, pp.1-9.
10. Patel, V.K. and Sharma, S., 2021. Effect of oxide supports on palladium-based catalysts for NO reduction by H_2-SCR. *Catalysis Today*, *375*, pp.591-600.
11. Pu, Z.Y., Lu, J.Q., Luo, M.F. and Xie, Y.L., 2007. Study of oxygen vacancies in $Ce_{0.9}Pr_{0.1}O_{2-\delta}$ solid solution by in situ X-ray diffraction and in situ Raman spectroscopy. *The Journal of Physical Chemistry C*, *111*(50), pp.18695-18702.
12. Wu, Z., Jin, R., Liu, Y. and Wang, H., 2008. Ceria modified MnO_x/TiO_2 as a superior catalyst for NO reduction with NH_3 at low-temperature. *Catalysis Communications*, *9*(13), pp.2217-2220.
13. Chang, H., Chen, X., Li, J., Ma, L., Wang, C., Liu, C., Schwank, J.W. and Hao, J., 2013. Improvement of activity and SO_2 tolerance of Sn-modified MnO_x–CeO_2 catalysts for NH_3-SCR at low temperatures. *Environmental science & technology*, *47*(10), pp.5294-5301.
14. Qingya, L., Zhenyu, L. and Chengyue, L., 2006. Adsorption and activation of NH_3 during selective catalytic reduction of NO by NH_3. *Chinese Journal of Catalysis*, *27*(7), pp.636-646.
15. Li Wei, Zhang Cheng, Li Xin, Tan Peng, Zhou Anli, Fang Qingyan and Chen Gang, 2018. Evaluation and characterization of Ho-modified Mn–Ce/TiO_2 catalysts for low-temperature denitration performance. Journal of Catalysis, 39 (10), pp.1653- 1663.

16. Liu, F., He, H., Ding, Y. and Zhang, C., 2009. Effect of manganese substitution on the structure and activity of iron titanate catalyst for the selective catalytic reduction of NO with NH_3. *Applied Catalysis B: Environmental*, *93*(1-2), pp.194-204.

17. Cao, Y., Zhang, C., Lv, L., Zhang, T., Chen, Y., Tang, S., Wang, Y. and Tang, W., 2023. Confinement effect and Hetero-interface enable High-Performing MnO_x/CeO_2 oxidation catalysts with exceptional sintering resistance: Morphology effect of ceria support. *Chemical Engineering Journal*, *462*, p.142257.

18. Wang, R., Mutinda, S.I. and Fang, M., 2013. One-pot hydrothermal synthesis and high temperature thermal stability of $Ce_xZr_{1-x}O_2$ nanocrystals. *RSC Advances*, *3*(42), pp.19508-19514.

19. Zhou, X., Ling, J., Sun, W. and Shen, Z., 2017. Fabrication of homogeneously Cu^{2+}/La^{3+}-doped CeO_2 nanosheets and their application in CO oxidation. *Journal of Materials Chemistry A*, *5*(20), pp.9717-9722.

20. Liyanage, A.D., Perera, S.D., Tan, K., Chabal, Y. and Balkus Jr, K.J., 2014. Synthesis, characterization, and photocatalytic activity of Y-doped CeO_2 nanorods. *Acs Catalysis*, *4*(2), pp.577-584.

21. Gao, R., Zhang, D., Maitarad, P., Shi, L., Rungrotmongkol, T., Li, H., Zhang, J. and Cao, W., 2013. Morphology-dependent properties of MnO_x/ZrO_2–CeO_2 nanostructures for the selective catalytic reduction of NO with NH_3. *The Journal of Physical Chemistry C*, *117*(20), pp.10502-10511.

22. Chen, L., Ren, S., Liu, L., Su, B., Yang, J., Chen, Z., Wang, M. and Liu, Q., 2022. Catalytic performance over Mn-Ce catalysts for NH_3-SCR of NO at low temperature: Different zeolite supports. *Journal of Environmental Chemical Engineering*, *10*(2), p.107167.

23. WU, X.M., NI, K.W., YU, X.L. and Ning, Z.H.A.O., 2020. In-situ DRIFTs study on different exposed facets of VO_x-MnO_x/CeO_2 catalysts for low-temperature NH_3-SCR. *Journal of Fuel Chemistry and Technology*, *48*(2), pp.179-188.

24. Zhang, B., Zhang, S. and Liu, B., 2020. Effect of oxygen vacancies on ceria catalyst for selective catalytic reduction of NO with NH_3. *Applied Surface Science*, *529*, p.147068.

25. Jiang, Z., Wang, Q. and Cai, Y., 2022. Enhanced Catalytic Activity and SO_2/H_2O Tolerance for Selective Catalytic Reduction of NO_x with NH_3 over Titanate Nanotubes Supported MnO_x–CeO_2 Catalyst at Low Temperature. *Catalysis Surveys from Asia*, *26*(3), pp.161-173.

26. Wang, H., Wang, L., Luo, Q., Zhang, J., Wang, C., Ge, X., Zhang, W., and Xiao, F.S., 2022. Two-dimensional manganese oxide on ceria for the catalytic partial oxidation of hydrocarbons. *Chemical Synthesis*, *2*(1), p.2.

27. Mingshan, C.U.I., Yuan, L.I., Xinquan, W.A.N.G., Jun, W.A.N.G. and Meiqing, S.H.E.N., 2013. Effect of preparation method on MnO_x-CeO_2 catalysts for NO oxidation. *Journal of Rare Earths*, *31*(6), pp.572-576.

28. Kang, M., Park, E.D., Kim, J.M. and Yie, J.E., 2007. Manganese oxide catalysts for NO_x reduction with NH_3 at low temperatures. *Applied catalysis A: general*, *327*(2), pp.261-269.